



Short-wavelength reverberant wave systems for physical realization of reservoir computing

Shukai Ma ^{1,*}, Thomas M. Antonsen,^{2,3} Steven M. Anlage ^{1,3} and Edward Ott^{2,3}

¹Quantum Materials Center, Department of Physics, University of Maryland, College Park, Maryland 20742, USA

²Department of Physics, University of Maryland, College Park, Maryland 20742, USA

³Department of Electrical and Computer Engineering, University of Maryland, College Park, Maryland 20742-3285, USA



(Received 11 October 2021; revised 28 January 2022; accepted 29 April 2022; published 31 May 2022)

Machine learning (ML) has found widespread application over a broad range of important tasks. To enhance ML performance, researchers have investigated computational architectures whose physical implementations promise compactness, high-speed execution, physical robustness, and low-energy cost. Here, we experimentally demonstrate an approach that uses the high sensitivity of reverberant short-wavelength waves for physical realization and enhancement of computational power of a type of ML known as reservoir computing (RC). The potential computation power of RC systems increases with their effective size. We here exploit the intrinsic property of short-wavelength reverberant wave sensitivity to perturbations to expand the effective size of the RC system by means of spatial and spectral perturbations. Working in the microwave regime, this scheme is tested experimentally on different ML tasks. Our results indicate the general applicability of reverberant wave based implementations of RC and of our effective reservoir size expansion techniques.

DOI: [10.1103/PhysRevResearch.4.023167](https://doi.org/10.1103/PhysRevResearch.4.023167)

I. INTRODUCTION

Machine learning (ML) algorithms have demonstrated the capability to perform a variety of tasks without being constructed with specific knowledge of the rules governing the task [1,2]. Important ML performance metrics, such as speed and energy efficiency, depend on the computing platform on which the ML algorithm operates. Accordingly, researchers have been motivated to find platforms and associated algorithms that optimize these metrics. In this regard, reservoir computing (RC) [3–6], a type of ML that we describe in Sec. II, has attracted attention because it can be realized in a variety of physical forms [7–20].

Based on the preceding motivation, we present in Sec. III an implementation of reservoir computing [4,5,12,21–24] that utilizes the complex response of short-wavelength modes in a reverberant cavity as the reservoir. When the wavelength of the fields in a cavity is much smaller than the size of the cavity, the wave field has effectively a high degree of freedom. Equivalently, in this “short-wavelength” regime the field can be thought of as a superposition of many modes: the number of which is determined by the bandwidth of the time-dependent signals to be produced and the spectral mode density of the cavity. This number of participating modes characterizes the effective amount of information contained in a specification of the reservoir state at a given time. As such, it

provides an upper limit on the information handling capacity and computational power of the RC. In practice, however, this upper limit may far exceed what is actually realized. We shall loosely refer to the realized number as the RC “size.”

In this paper, we present a proof-of-principle experimental demonstration of a short wavelength wave based RC system operating in the microwave regime. Most importantly, by exploiting the high degree of freedom of the wave fields, and by introducing several new reservoir enhancement techniques (RETs), we show that a measure of the size of the RC system can be made large, thus greatly enhancing the RC computational power. The potential computing power and versatility of wave-based RC systems are demonstrated and assessed in Sec. V through experimental and numerical tests on several benchmark tasks.

II. CONVENTIONAL RESERVOIR COMPUTING

Reservoir computing is a general type of ML whose structure, in the case of continuous-time operation, can be specified as follows. Input variables, in the form of a time (t) dependent vector $u(t)$, drive the evolution of a reservoir state $\hat{r}(t)$. The reservoir state \hat{r} is typically a high dimensional vector, and the input u is a much lower dimensional signal vector to which \hat{r} responds. [In our case, \hat{r} represents the field within the wave-confining structure, e.g., the microwave cavity shown in Fig. 1(a).]

The reservoir state evolves according to a reservoir dynamical system f ,

$$\frac{d\hat{r}(t)}{dt} = f(\hat{r}(t), u(t)). \quad (1)$$

In Eq. (1), it is assumed that f satisfies the “echo-state” property [4,5], which requires that for any input time series

*skma@umd.edu

Published by the American Physical Society under the terms of the [Creative Commons Attribution 4.0 International](https://creativecommons.org/licenses/by/4.0/) license. Further distribution of this work must maintain attribution to the author(s) and the published article's title, journal citation, and DOI.

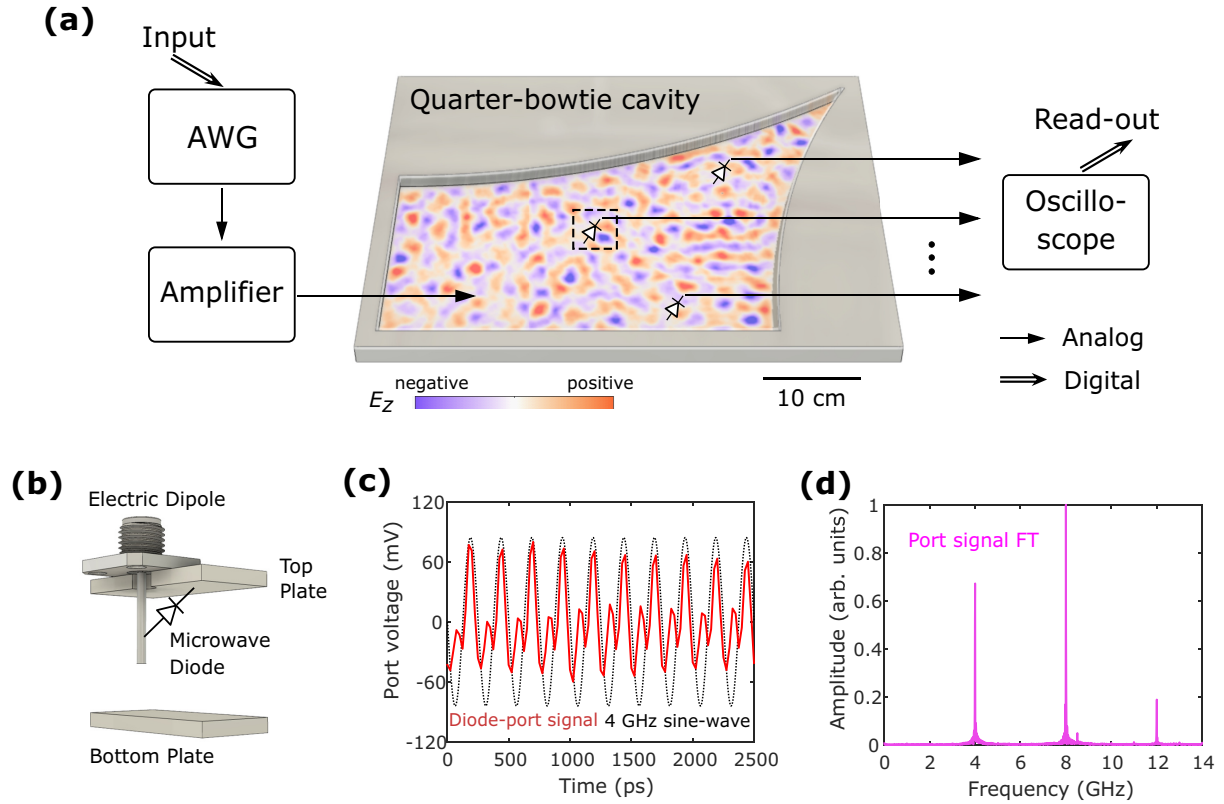


FIG. 1. Reverberant wave systems for reservoir computing. (a) Schematic of the experimental setup. The input information is transferred from a laboratory computer to the AWG and injected into the chaotic enclosure through a simple electric dipole antenna. Several diode-loaded antennas are used to probe the EM field, whose voltage signals are measured by the oscilloscope and further transferred to the laboratory computer and stored. The cavity shown in panel (a) is thin in the vertical, z direction, and has a shape in the (x, y) directions in which the bottom and left walls are straight lines and the upper and right walls are circular arcs. This leads to a purely vertical electrical field $E_z(x, y)$ whose complex two-dimensional spatial distribution is shown in panel (a) via the blue-to-red color coding within the cavity. (b) Schematic of the diode-loaded port. (c) The dynamics of diode-port voltage (red) under single-frequency (4 GHz) input wave (black) injected at the linear input port. (d) The Fourier transform (FT) of the diode-port signal shown in (c).

$u(t)$, $\hat{r}(t)$ becomes independent of the initial condition $\hat{r}(0)$ as t becomes large. A time series of output vectors $r(t)$ of dimension N_r is derived from the reservoir state $\hat{r}(t)$ via a function g ,

$$r(t) = g(\hat{r}(t)). \quad (2a)$$

The overall RC system output, denoted by a vector $s(t)$, is taken to depend linearly on the vector $r(t)$,

$$s(t) = W r(t), \quad (2b)$$

where W is a rectangular matrix, and the dimension N_r of $r(t)$ is typically large compared with the dimension of the vector $s(t)$. The elements of the matrix W are viewed as adjustable parameters whose values are chosen through a “training” procedure, whereby, based on training data consisting of examples (u, s') of inputs $u(t)$ and the corresponding desired resulting outputs $s'(t)$, W is determined by minimizing the deviations of $s(t)$ (the actual RC output) from $s'(t)$. Heuristically, the basic assumptions of reservoir computing are that, (i) if the dimension N_r is large, and the N_r individual elements of the time-dependent vector $r(t)$ evolve in diverse ways, then the best fit of $s(t) = W r(t)$ to $s'(t)$ will indeed be a very good approximation to the time-varying vector $s'(t)$; and (ii) following training, the RC system outputs will continue

to give a good approximation to the outputs $s'(t)$ that would be desired for the post-training inputs. Based on item (i) we shall view N_r as quantifying the notion of RC system size. Operationally, item (ii) is promoted by the use of training regularization (typically, for RC, ridge regression) meant to prevent overfitting [5]. In general, either the function f , or the function g , or both should be nonlinear to allow the RC system to perform a wide variety of nonlinear tasks [25]. We note that, by virtue of the linear relation $s = W r$, the training of an RC system reduces to a simple linear regression. Thus, the training of an RC can be very fast [26].

III. REVERBERANT WAVE RC

Figure 1 shows the proof-of-principle experimental microwave reverberant wave based RC system considered in this paper. In Fig. 1(a), digital input signals are transformed into analog waveforms by an Tektronix 70000A AWG (arbitrary waveform generator) and stored for both the training and testing time-series data sets. These analog waveforms are exactly the same as the digital input signal stream. Note that no signal formatting or masking is applied at this step. The waveform is then amplified by the RF-Lambda 2-18GHz

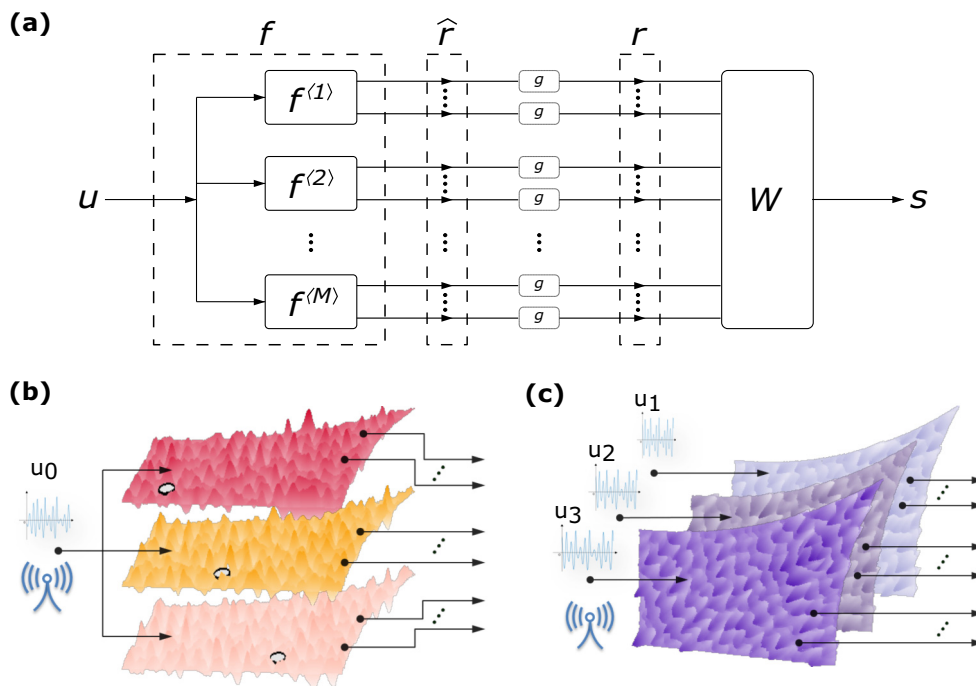


FIG. 2. Reservoir enhancement techniques (RETs). (a) The proposed architecture for f and r [Eqs. (3) to (5)]. (b) and (c) show schematics of the boundary-condition method and the frequency-stirring method, respectively. The first method may be realized by the translation of a metallic perturber shown as the cylinders. Under the same input waveform u_0 , uniquely different evolutions of the EM fields inside the enclosure area are created by means of translating the perturber to new locations. In (c), the frequency-stirring technique utilizes small changes of center frequency of a given input waveform to create new wave field configurations. In the experiment, the input wavelet is stretched or shrunk by different amounts (forming the inputs u_1, u_2 , and u_3) in order to shift the center frequency. Each output arrow of panels (b) and (c) represents one of the N_r components $r^{(i)}$ of the vector r .

amplifier (RFLUPA0218G5), and injected into a wave-chaotic microwave cavity with an area $A = 0.115 \text{ m}^2$ [27–31]. The shape of the cavity is formed from two straight walls intersecting at a right angle and two additional circular arc-shaped walls. The characteristic length of the cavity is of $A^{0.5} \sim 35 \text{ cm}$ and thus the cavity is electrically large compared to the nominal operating wavelength ($\sim 5 \text{ cm}$). With a height of $d = 0.79 \text{ cm}$, the cavity can be considered to be quasi-2D because the electric field is polarized in the z direction for $f < c/(2d) = 18.9 \text{ GHz}$. Microwave absorbers are employed inside to alter the fading memory of the system. For tasks running at $\sim \text{GHz}$ rates, the cavity decay time is in the $\sim \text{ns}$ range. The port voltage signals are measured with an oscilloscope (Agilent DSO91304A) with a sampling rate of 40 GS/s.

The timescale of the input (signals vary on the $\sim 100 \text{ ps}$ scale) is such that the input stream will excite hundreds of cavity eigenmodes. The enclosure is designed to act as a two-dimensional “quarter bow-tie shaped” geometry so that the rays (straight-line orbits between specular reflection from the cavity walls) show chaotic dynamics (i.e., ray orbits with nearby initial conditions typically diverge exponentially as they propagate and experience successive reflections from the cavity’s enclosing walls). The EM field emerges as the real-time superposition of all system modes, sampled at discrete locations (the N_r output ports) in the system. To include non-linearity into the otherwise linear cavity system, we installed high switching speed diodes (Infineon BAS7004) at the output ports [Fig. 1(b)] [29]. This nonlinearity is demonstrated by

the port voltage signal distortion of a sinusoidal wave injected at the linear input port [Fig. 1(c)] and the resulting higher-harmonic responses [Fig. 1(d)]. Thus, the complexity of the reverberant wave reservoir is ensured by the short-wavelength sensitivity property of the cavity fields and the nonlinear elements connected at the ports.

In analogy with the conventional RC, the reservoir layer $\hat{r}(t)$ is the field distribution within the cavity at time t , the function f describes the field dynamics in the cavity and to some extent the action of the diodes at the ports, N_r is the number of available measurement channels, and g is the nonlinear function realized by the ports and diodes [16]. The geometrical simplicity of the cavity is in marked contrast to network implementations of RC where the complexity of the function f is built from a complex network topology. This simplicity suggests the possibility of fabrication, and mechanical robustness advantages of the wave-chaos approach.

Here the N_r diode-loaded ports serve as the observable reservoir nodes and hence a measure of the RC size. The N_r signals at the ports are recorded on the oscilloscope and transferred to a laboratory computer for off-line training [Fig. 1(a)]. The number of wave outputs (N_r) of the wave-based RC can, in principle, be increased up to the resolution limit of the operating wavelength. Challenges, however, arise because the total number of measurement ports (N_r) in a physical RC may be limited in practice. For example in our experiment, the number of output ports is limited by the number of recording channels on the oscilloscope (Fig. 1).

IV. RESERVOIR ENHANCEMENT TECHNIQUES

To address the issue of the limited number of output ports and replicate the RC performance of a cavity with more ports, we introduce what we call reservoir enhancement techniques (RETs). To formulate our description of RETs, we consider a specific convenient structure for the N_r -dimensional function $f(\hat{r}, u)$ in Eq. (1). In particular, we let $N_r = MN'_r$ and write the N_r -dimensional vector $r = g(\hat{r})$ as the concatenation of M component vectors each of dimension N'_r . Denoting these component vectors $r^{(1)}, r^{(2)}, \dots, r^{(M)}$, we have

$$r = [r^{(1)}; r^{(2)}; \dots; r^{(M)}]. \quad (3)$$

Correspondingly, we write f as

$$f(\hat{r}, u) = [f^{(1)}(\hat{r}^{(1)}, u); f^{(2)}(\hat{r}^{(2)}, u); \dots; f^{(M)}(\hat{r}^{(M)}, u)], \quad (4)$$

so that

$$\hat{r}_{n+1}^{(i)} = f^{(i)}(\hat{r}_n^{(i)}, u(t)). \quad (5)$$

Thus, each of the $\hat{r}^{(i)}$ evolves independently of the others, except from the mutual dependence on the input stream $u(t)$. Comparing Eq. (5) with Eq. (1), we consider each of the components $\hat{r}^{(i)}$ of \hat{r} to be the wave field distribution in a hypothetical cavity described by $f^{(i)}$. The idea, illustrated in Fig. 2(a), is to increase the diversity of the vector r by increasing its dimension above that for $M = 1$ (ideally by the factor M) so that $W r$ can better fit the desired time dependence of s . Accordingly, we desire the $\hat{r}^{(i)}$ to be very different for different i , which implies that the $f^{(i)}$ must be different for different i .

This seems to present a challenge for physical implementation, as it seems to require M different physically constructed cavities. However, we can achieve Eq. (4) with very different $f^{(i)}$ and large M by taking advantage of the hallmark property of short-wavelength reverberant waves, namely, extreme sensitivity of the field distribution within the cavity, and hence also $f^{(i)}$, to small changes in the cavity boundaries. Thus, in our experiments in this paper we will make use of this sensitivity through two alternative techniques allowing physical implementation of Eqs. (3) and (5) using a *single* cavity. We call these two techniques the “boundary-condition method” [Fig. 2(b)] and the “frequency-stirring method” [Fig. 2(c)]. As a proof-of-principle demonstration of the boundary-condition method, we place a small conducting circular cylinder in the cavity and move it to different locations, each location corresponding to a different $f^{(i)}$. In the frequency-stirring method we uniformly scale the duration of the input signal time dependence by a factor $\beta^{(i)}$, $t \rightarrow \beta^{(i)} t$; since the medium within the cavity is air (essentially equivalent to vacuum), the waves are nondispersive, and scaling time by $\beta^{(i)}$ is equivalent to scaling distances characterizing the shape of the cavity walls uniformly by the factor $(\beta^{(i)})^{-1}$. For an input waveform centered at $f_0 = 4$ GHz, we translate the perturber (a conducting cylinder of radius 1.5 cm and height 0.75 cm) by 1 cm ($\sim 0.2\lambda_0$) or shift the center frequency f_0 by $\Delta f = 100$ MHz (~ 3 resonator eigenmodes) to create a new reservoir.

Figures 2(b) and 2(c) show snapshots of the complex electric field E_z landscape within the cavity obtained from time-domain simulations. These simulations confirm that small variations of system boundary conditions, as well as small input time stretching or shrinking, result in drastically

different wave field spatial distributions. Virtual new unit reservoirs each having distinct temporal dynamics are thus created. The application of RET does require a longer operational time to conduct measurements with a single reservoir, and a requirement to store all measured results and combine them later. However, our RET serves as a unique way to enhance the reservoir size without making new hardware, new ports, or even new cable connections inside the system. Although we have not implemented them in the experiments reported in this paper, there are other ways of physically achieving Eqs. (3)–(5) with a single cavity. For example, one attractive possibility is to place a metasurface with electronically programmable surface impedance elements on a portion of the cavity wall [32–35] and electronically switch between many different surface impedance configurations. This may be regarded as an electronic implementation of our boundary-condition method which does not utilize the practically problematic process of physically moving a perturbing object within the cavity. We note that related techniques for enhancing the reservoir size are also proposed in Refs. [23,36–38].

V. RESULTS

We have experimentally investigated the effectiveness of our reverberant wave approach to implementing RC on several different tasks. Ensembles of new reservoirs are created by translating a metallic perturber and/or changing the oscillation period of the input signal from the AWG. In our experiment, a combined RC of size N_r is given by

$$N_r = N_0 N_b N_f, \quad (6)$$

where N_0 , N_b , and N_f represent the number of measurement channels, the number of applications of the boundary-condition perturbation RET, and the number of applications of the frequency-stirring RET, respectively.

For the experiments described below we used the bow-tie cavity with $N_0 = 3$ output ports. Without using RETs we find that, for all of the 5 tasks tested, the RC system fails to give useful results. However, with RET implemented, the performance of all 5 tasks improves, becoming better as the effective RC system size N_r increases [Figs. 3(d), 4(b), 4(d), and 4(f)]. For the 5 examples tested we found that using RET to sufficiently boost N_r resulted in excellent performance. In the rest of this section we give results of our tests.

Example 1: The observer task applied to the continuous-time chaotic Rössler attractor. For the observer task [6], the RC system is expected to infer the time variation of unobserved state variables of a dynamical system [in this example, the $y(t)$ and $z(t)$ components of the chaotic Rössler system] based only on observations of a subset of the system state variables in this example the Rössler $x(t)$ component. The Rössler system is governed by these equations,

$$\begin{aligned} \dot{x} &= -y - z, \\ \dot{y} &= x + ay, \\ \dot{z} &= b + z(x - c), \end{aligned} \quad (7)$$

where $a = 0.5$, $b = 2.1$, $c = 3.5$, and the overdot denotes derivative with respect to time.

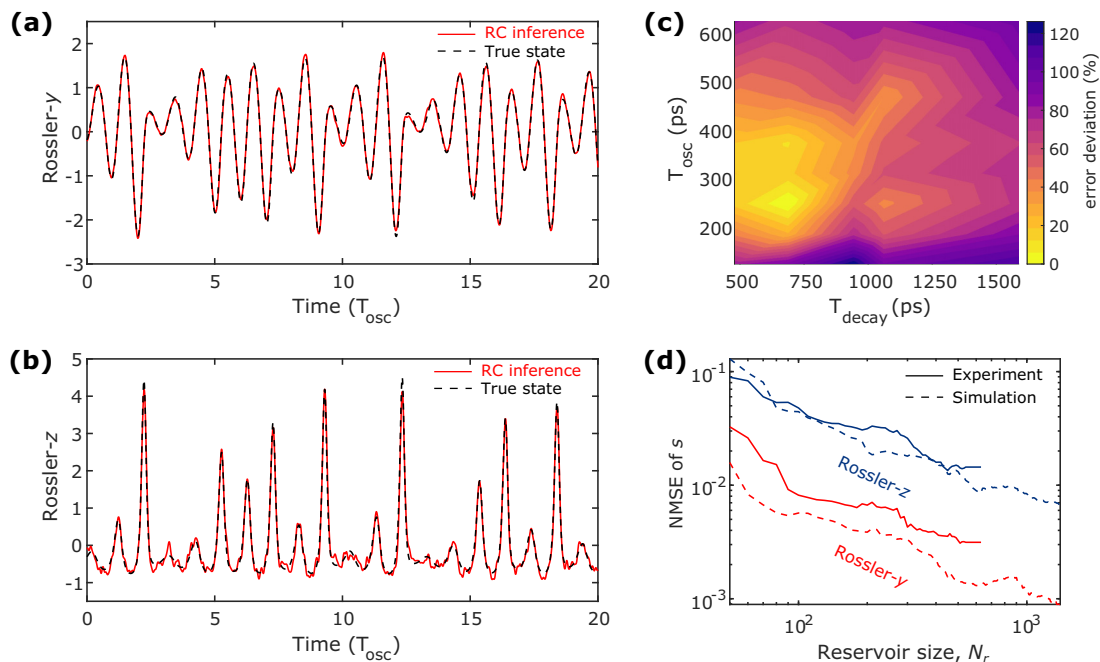


FIG. 3. Observer task test results for the Rössler system. (a) and (b) The RC inferences of $y(t)$ and $z(t)$ (red solid line) versus time in units of T_{osc} agree with their true values (black dashed line). (c) A plot at $N_r = 90$ ($N_0 = 3$, $N_b = 30$) of the percent deviation of the Rössler observer task NMSE, $\sum_n |s(t) - s'(t)|^2 / \sum_n |s(t)|^2$, from the NMSE with optimal parameters $(T_{\text{osc}}, T_{\text{decay}}) = (250, 700)$ as a function of the input duration T_{osc} and the system decay time T_{decay} . (d) The normalized mean-squared error in s versus N_r , the dimension of r , which is varied, e.g., for the experimental (solid) curves, by starting at a maximum value of $N_r = 630$ (corresponding to $N_0 = 3$, $N_b = 30$, $N_f = 7$), and then randomly removing virtual outputs to successively lower N_r .

Like other ML methods, this prediction task is carried out without knowledge of the equations of motion of the Rössler system, using only a finite duration of data of all three components for training. The performance of the RC inference $s = (y, z)$ is evaluated using the normalized mean-squared error, e.g., defined for the y variable as $\text{NMSE} = \sum_n [y_n - y'_n]^2 / \sum_n y_n^2$, where y' and y denote true and RC-inferred values, respectively, and n is the time index of the testing set data, $y_n = y(n \Delta t)$, with Δt chosen small enough compared to T_{osc} (the timescale for the variation of the Rössler state) that y at the discrete times $n \Delta t$ traces out a good approximation of the continuous variation of $y(t)$. The NMSE of the Rössler z component is computed analogously. Here T_{osc} is defined by first noting that the frequency power spectrum of the RC input (here the Rössler x series) shows a pronounced well-defined lowest spectral component, and T_{osc} is defined as the period corresponding to the frequency at the peak of this spectral component. In the training period, the input is the Rössler x component with ~ 200 oscillation periods T_{osc} , and the testing period includes ~ 50 periods. We also note that we can vary T_{osc} by application of the previously mentioned time scaling of the RC system input ($t \rightarrow \beta t$). With RET, a reservoir of $N_r = 630$ output channels is created and this RC achieves $\text{NMSE} = (0.003, 0.014)$ for inference of the Rössler y and z components, respectively. This combined RC size ($N_r = 630$) is achieved from 30 applications of the RET boundary method ($N_b = 30$) and 7 applications of the RET frequency-stirring method ($N_f = 7$), which, from Eq. (6), when combined with the 3 existing ports of the cavity ($N_0 = 3$), yields $N_r = 3 \times 30 \times 7 = 630$. In Figs. 3(a) and 3(b) the inferred Rössler y and

z components, obtained using the $N_r = 630$ RC, are plotted as red solid lines and accurately reproduce their corresponding true values (black dashed lines).

Figure 3(c) shows a heat map of the reservoir performance, with $N_r = 90$, in the inference of $s = (y, z)$ versus the reservoir parameters T_{osc} and T_{decay} . Here T_{decay} denotes the exponential damping time of waves of frequency $2\pi/T_{\text{osc}}$ in the undriven cavity, and is varied by placing dissipative material within the cavity. For an empty cavity, the measured decay time is ~ 2.14 ns. Thus the shortest decay time (left boundary of the heat map) corresponds to the case of the most lossy cavity. As shown in Fig. 3(d), as N_r increases via applications of RETs (see figure caption), the RC performance is greatly improved.

Example 2: The observer task for the discrete-time chaotic Hénon map. Results for the RC observer task applied to the two-dimensional discrete-time chaotic Hénon map, $(x_{n+1}, y_{n+1}) = (1 - 1.4x_n^2 + y_n, 0.3x_n)$, are shown in Figs. 4(a) and 4(b), where the variable x is observed and y is inferred. Each input value of the discrete x series is sampled for $T_{\text{bin}} \sim 60$ ps. The decay time of the system is fixed at $T_{\text{decay}} \sim 600$ ps. The training waveform of the Hénon map has a length of 4000 time steps, and the testing waveform is set to 1000 bins. We see that the RC-inferred values of y (plotted in blue) agree well with the true values (plotted as a dashed red curve). For these results, RETs yielding $N_r = 540$ (see figure caption) were employed.

Example 3: The nonlinear channel equalization task. For the nonlinear channel equalization (NCE) task, the goal is to recover a random 4-level symbol sequence from a noisy

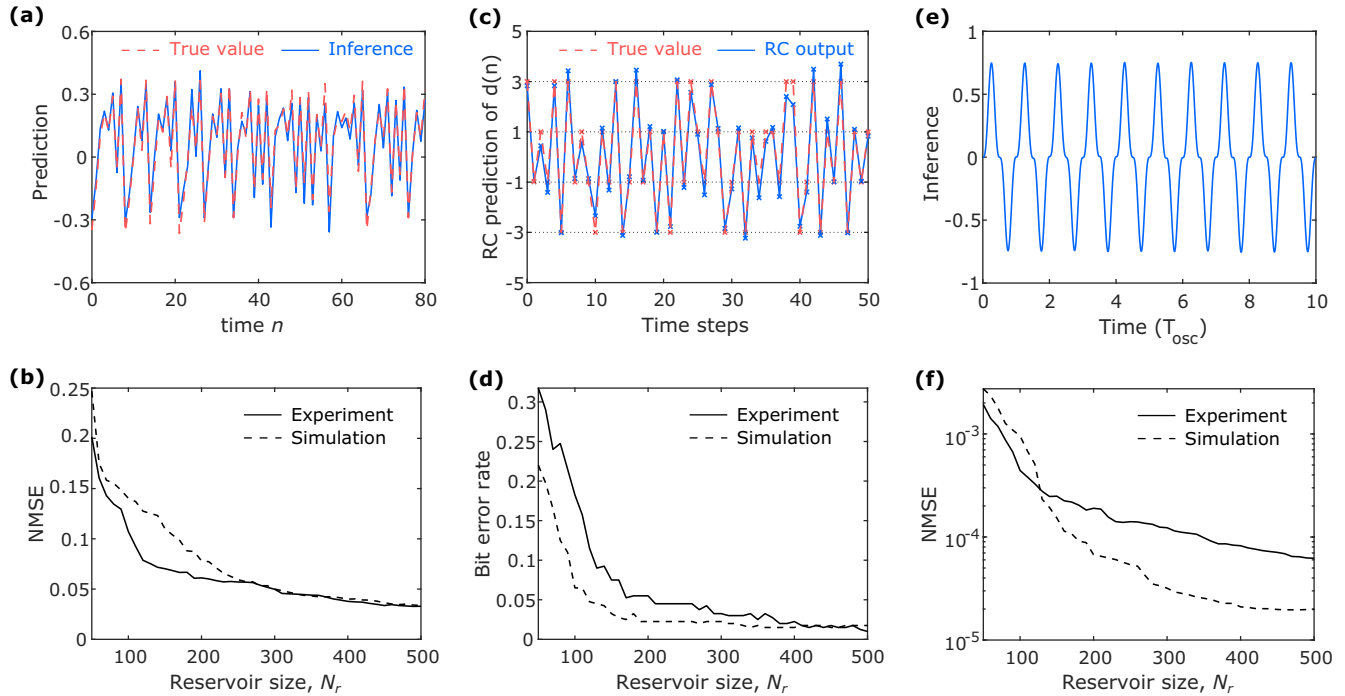


FIG. 4. Hénon map observer task performance. (a) The true orbit y_n (dashed red) and its RC inference (blue) as a function of time step n for an RC size of $N_r = 540$ obtained using 3 cavity ports, 30 implementations of the boundary RET, and 6 implementations of the frequency-stirring RET ($N_r = 3 \times 30 \times 6 = 540$). (b) The RC inference normalized error versus the reservoir size, N_r . Nonlinear channel equalizer (NCE) task performance. (c) The RC performances (blue) for the NCE task. The targets are shown as red dashed lines. In (d), we show the simulated (dashed) and experimental (solid) RC performance as a function of the reservoir size N_r . Function simulator task performance. (e) The RC performance (blue) for the function simulator task. In (f), we show the simulated (dashed) and experimental (solid) RC performance as a function of the dimension of the reservoir.

sequence which simulates the received signal sent through a nonlinear multipath RF channel. For the 4-level symbol sequence, a random series $d(n)$ is chosen between the levels $\{-3, -1, 1, 3\}$, and the RF channel signal is assumed to be $q(n) = 0.08d(n+2) - 0.12d(n+1) + d(n) + 0.18d(n-1) - 0.1d(n-2) + 0.091d(n-3) - 0.05d(n-4) + 0.04d(n-5) + 0.03d(n-6) + 0.01d(n-7)$. The RC system input for this NCE task is the channel signal $q(n)$, and the task is to retrieve the original four-level random $d(n)$ series. In the experiment, an input speed of $T_{\text{bin}} \sim 60$ ps is adopted, and the training/testing set includes 4000/1000 time steps, respectively. The decay time of the system is fixed at $T_{\text{decay}} \sim 600$ ps. The direct RC output is regularized to the nearest level. Results for this test are shown in Figs. 4(c) and 4(d).

Example 4: The function simulator task. For the function simulator task, the RC is expected to output any periodic waveform that is desired. For this purpose, we take the input to be a sinusoidal waveform with the period of the desired waveform. In our test example we take the desired waveform to be the cube of the sine wave, and we train the RC system to give this output. The decay time of the system is fixed at $T_{\text{decay}} \sim 600$ ps. We employ a 4 GHz sine wave input with a duration of ~ 300 oscillation periods. The lengths of the training and testing sets are set to an 80 : 20 ratio. Results for this test show very good agreement between the RC output waveform and the target [Figs. 4(e) and 4(f)]. (We have also

confirmed that the wave-based RC is able to generate other types of input functions, including two-tone and three-tone signals.)

Example 5: The NARMA-10 task. For the 10-time-step nonlinear autoregressive moving average (NARMA-10) task, the input stream $u(n)$ is a random series drawn from the interval $[0, 0.5]$. The target output is computed from the following 10th-order nonlinear relationship: $y(n+1) = 0.3y(n) + 0.05y(n)[\sum_{i=0}^9 y(n-i)] + 1.5u(n-9) \times u(n) + 0.1$. Its complex behavior and a 10-state memory requirement make the NARMA-10 task a popular benchmark test for both software and hardware RC [14,18]. The training waveform has a length of 4000 random values, and the testing waveform is set to 1000 values. With optimal system parameters [cross in Fig. 5(b)], a RC with $N_r = 90$ achieves a performance of $\text{NMSE} = 0.034$ which compares favorably with that reported in several recent photonic hardware RC implementations (e.g., see [18]). The optimized performance island occurs when $T_{\text{decay}} \sim 9T_{\text{bin}}$ [Fig. 5(b)]. This empirical observation agrees nicely with the setup of the NARMA-10 task where each output time step is determined by its 10 previous inputs, thus demonstrating the complex memory capacity of the wave-based RC. In the experiment, the input is a time-domain waveform where each value is sampled for $T_{\text{bin}} \sim 60$ ps. We note that such choices of input waveform speeds are limited by the sampling speed of both the AWG and the oscilloscope.

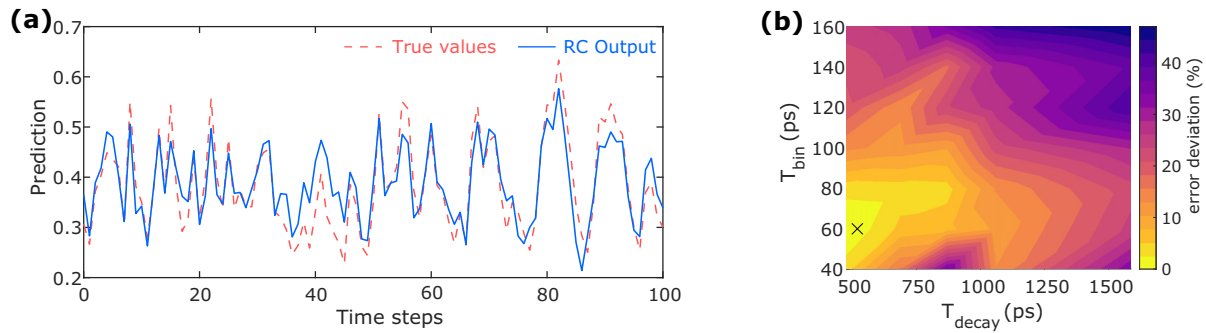


FIG. 5. (a) NARMA-10 task testing set performance at the optimal system parameters from an RC size of $N_r = 90$ (obtained via the 3 cavity ports with 30 applications of the boundary RET), shown as the cross in (b). (c) shows the deviation of the NMSE for an $N_r = 90$ ($N_0 = 3$, $N_b = 30$) RC. The percent deviation is computed with respect to the NMSE of the optimal parameters $(T_{\text{bin}}, T_{\text{decay}}) = (60, 550)$ as a function of the input value duration T_{bin} and the system decay time T_{decay} .

Besides experimental tests, we have also conducted electromagnetic (EM) numerical simulations in CST Microwave Studio of the physical RC with the same shape cavity, identical degree of system loss, and realistic model of the diodes. The high-dimensional combined RC is realized with the RETs, where the boundary-condition perturbation is realized using the cylindrical metallic perturber with the same dimension as the experimental one. As shown in Figs. 3(d), 4(b), 4(d), and 4(f), all of our experimental cases are faithfully simulated with EM simulation numerical tools. The accurate simulation capability of wave-based RC greatly benefits future RC optimization and follow-up studies.

We also point out that the ultimate realization of the proposed RC will have as many ports as needed to achieve a desired performance. Using full-wave simulations, we tested a version of the RC which has $N_r \gg 3$ ports installed in one single cavity and found good performance (not shown in the paper). In experiments, RET allows us to validate our wave-based RC concept under our limited measurement capabilities. It would otherwise be impossible for us to demonstrate our hardware RC concept. The RET concepts show that a reservoir consisting of a number of wave-based RCs running in parallel will also work. Similar combined RC configurations are also introduced in Refs. [20,22,23].

VI. CONCLUSION

Benefiting from the basic nature of short-wavelength reverberant wave systems, our RC scheme shows advantages in

its simplified physical structure and insensitivity to structural details. The computational performance of the wave-based RC, quantified by the testing set error for various benchmark tests, is greatly improved by the expansion of the reservoir size. We note that the efficacy of the output coupling matrix W may degrade as the RC scattering properties change over time (e.g., due to aging at very long time) [39,40]. However, this performance drift can be quickly recalibrated because the training of the RC is fast.

In summary, we have experimentally demonstrated a physical platform for reservoir computing utilizing the complex dynamics of waves, and found good agreement between experiments and simulations. By exploiting the fundamental property of the short-wavelength systems (i.e., extreme sensitivity of the wave field distribution to perturbations), we formulate techniques for expanding the size and computational power of wave-based RC. We further demonstrate the effectiveness of our approach by the successful execution of different benchmark tests. Our general scheme for enhancing the computational power of RC [Fig. 2(a)] may be of general use beyond application to wave-based RC.

ACKNOWLEDGMENTS

This work was supported by ONR under Grant No. N000141912481, AFOSR COE Grant No. FA9550-15-1-0171, and the Maryland Quantum Materials Center.

-
- [1] Y. LeCun, Y. Bengio, and G. Hinton, Deep learning, *Nature (London)* **521**, 436 (2015).
 - [2] G. Wetzstein, A. Ozcan, S. Gigan, S. Fan, D. Englund, M. Soljačić, C. Denz, D. A. B. Miller, and D. Psaltis, Inference in artificial intelligence with deep optics and photonics, *Nature (London)* **588**, 39 (2020).
 - [3] W. Maass, T. Natschläger, and H. Markram, Real-time computing without stable states: A new framework for neural computation based on perturbations, *Neural Comput.* **14**, 2531 (2002).
 - [4] H. Jaeger, Harnessing nonlinearity: Predicting chaotic systems and saving energy in wireless communication, *Science* **304**, 78 (2004).
 - [5] M. Lukoševičius and H. Jaeger, Reservoir computing approaches to recurrent neural network training, *Comput. Sci. Rev.* **3**, 127 (2009).
 - [6] Z. Lu, J. Pathak, B. Hunt, M. Girvan, R. Broomhead, and E. Ott, Reservoir observers: Model-free inference of unmeasured variables in chaotic systems, *Chaos* **27**, 041102 (2017).

- [7] C. Fernando and S. Sojakka, Pattern recognition in a bucket, in *European Conference on Artificial Life* (Springer, Berlin, 2003), pp. 588–597.
- [8] L. Appeltant, M. C. Soriano, G. Van der Sande, J. Danckaert, S. Massar, J. Dambre, B. Schrauwen, C. R. Mirasso, and I. Fischer, Information processing using a single dynamical node as complex system, *Nat. Commun.* **2**, 468 (2011).
- [9] L. Larger, M. C. Soriano, D. Brunner, L. Appeltant, J. M. Gutiérrez, L. Pesquera, C. R. Mirasso, and I. Fischer, Photonic information processing beyond Turing: An optoelectronic implementation of reservoir computing, *Opt. Express* **20**, 3241 (2012).
- [10] Y. Paquot, F. Duport, A. Smerieri, J. Dambre, B. Schrauwen, M. Haelterman, and S. Massar, Optoelectronic reservoir computing, *Sci. Rep.* **2**, 287 (2012).
- [11] M. C. Soriano, D. Brunner, M. Escalona-Morán, C. R. Mirasso, and I. Fischer, Minimal approach to neuro-inspired information processing, *Front. Comput. Neurosci.* **9**, 68 (2015).
- [12] D. Canaday, A. Griffith, and D. J. Gauthier, Rapid time series prediction with a hardware-based reservoir computer, *Chaos* **28**, 123119 (2018).
- [13] F. Laporte, A. Katumba, J. Dambre, and P. Bienstman, Numerical demonstration of neuromorphic computing with photonic crystal cavities, *Opt. Express* **26**, 7955 (2018).
- [14] G. Tanaka, T. Yamane, J. B. Héroux, R. Nakane, N. Kanazawa, S. Takeda, H. Numata, D. Nakano, and A. Hirose, Recent advances in physical reservoir computing: A review, *Neural Networks* **115**, 100 (2019).
- [15] F. Laporte, Novel architectures for brain-inspired photonic computers, Ph.D. thesis, Universiteit Gent, 2020.
- [16] M. Rafayelyan, J. Dong, Y. Tan, F. Krzakala, and S. Gigan, Large-Scale Optical Reservoir Computing for Spatiotemporal Chaotic Systems Prediction, *Phys. Rev. X* **10**, 041037 (2020).
- [17] G. Marcucci, D. Pierangeli, and C. Conti, Theory of Neuromorphic Computing by Waves: Machine Learning by Rogue Waves, Dispersive Shocks, and Solitons, *Phys. Rev. Lett.* **125**, 093901 (2020).
- [18] Y. K. Chembo, Machine learning based on reservoir computing with time-delayed optoelectronic and photonic systems, *Chaos* **30**, 013111 (2020).
- [19] U. Paudel, M. Luengo-Kovac, J. Pilawa, T. J. Shaw, and G. C. Valley, Classification of time-domain waveforms using a speckle-based optical reservoir computer, *Opt. Express* **28**, 1225 (2020).
- [20] X. Porte, A. Skalli, N. Haghighi, S. Reitzenstein, J. A. Lott, and D. Brunner, A complete, parallel and autonomous photonic neural network in a semiconductor multimode laser, *J. Phys.: Photonics* **3**, 024017 (2021).
- [21] J. Torrejon, M. Riou, F. A. Araujo, S. Tsunegi, G. Khalsa, D. Querlioz, P. Bortolotti, V. Cros, K. Yakushiji, A. Fukushima, H. Kubota, S. Yuasa, M. D. Stiles, and J. Grollier, Neuromorphic computing with nanoscale spintronic oscillators, *Nature (London)* **547**, 428 (2017).
- [22] K. Nakajima, K. Fujii, M. Negoro, K. Mitarai, and M. Kitagawa, Boosting Computational Power through Spatial Multiplexing in Quantum Reservoir Computing, *Phys. Rev. Appl.* **11**, 034021 (2019).
- [23] Y. Zhong, J. Tang, X. Li, B. Gao, H. Qian, and H. Wu, Dynamic memristor-based reservoir computing for high-efficiency temporal signal processing, *Nat. Commun.* **12**, 408 (2021).
- [24] D. J. Gauthier, E. Bollt, A. Griffith, and W. A. S. Barbosa, Next generation reservoir computing, *Nat. Commun.* **12**, 5564 (2021).
- [25] L. Grigoryeva and J.-P. Ortega, Echo state networks are universal, *Neural Networks* **108**, 495 (2018).
- [26] P. R. Vlachas, J. Pathak, B. R. Hunt, T. P. Sapsis, M. Girvan, E. Ott, and P. Koumoutsakos, Backpropagation algorithms and reservoir computing in recurrent neural networks for the forecasting of complex spatiotemporal dynamics, *Neural Networks* **126**, 191 (2020).
- [27] P. So, S. M. Anlage, E. Ott, and R. N. Oerter, Wave Chaos Experiments with and without Time Reversal Symmetry: GUE and GOE Statistics, *Phys. Rev. Lett.* **74**, 2662 (1995).
- [28] S. Hemmady, X. Zheng, E. Ott, T. M. Antonsen, and S. M. Anlage, Universal Impedance Fluctuations in Wave Chaotic Systems, *Phys. Rev. Lett.* **94**, 014102 (2005).
- [29] M. Zhou, E. Ott, T. M. Antonsen, and S. M. Anlage, Scattering statistics in nonlinear wave chaotic systems, *Chaos* **29**, 033113 (2019).
- [30] S. Ma, B. Xiao, Z. Drikas, B. Addissie, R. Hong, T. M. Antonsen, E. Ott, and S. M. Anlage, Wave scattering properties of multiple weakly coupled complex systems, *Phys. Rev. E* **101**, 022201 (2020).
- [31] S. Ma, S. Phang, Z. Drikas, B. Addissie, R. Hong, V. Blakaj, G. Gradoni, G. Tanner, T. M. Antonsen, E. Ott, and S. M. Anlage, Efficient Statistical Model for Predicting Electromagnetic Wave Distribution in Coupled Enclosures, *Phys. Rev. Appl.* **14**, 014022 (2020).
- [32] P. del Hougne, M. F. Imani, M. Fink, D. R. Smith, and G. Lerosey, Precise Localization of Multiple Noncooperative Objects in a Disordered Cavity by Wave Front Shaping, *Phys. Rev. Lett.* **121**, 063901 (2018).
- [33] C. C. Nadell, B. Huang, J. M. Malof, and W. J. Padilla, Deep learning for accelerated all-dielectric metasurface design, *Opt. Express* **27**, 27523 (2019).
- [34] B. W. Frazier, T. M. Antonsen, S. M. Anlage, and E. Ott, Wavefront shaping with a tunable metasurface: Creating cold spots and coherent perfect absorption at arbitrary frequencies, *Phys. Rev. Research* **2**, 043422 (2020).
- [35] C. Qian, B. Zheng, Y. Shen, L. Jing, E. Li, L. Shen, and H. Chen, Deep-learning-enabled self-adaptive microwave cloak without human intervention, *Nat. Photonics* **14**, 383 (2020).
- [36] L. Grigoryeva, J. Henriques, L. Larger, and J.-P. Ortega, Nonlinear memory capacity of parallel time-delay reservoir computers in the processing of multidimensional signals, *Neural Comput.* **28**, 1411 (2016).
- [37] M. Freiberger, S. Sackesyn, C. Ma, A. Katumba, P. Bienstman, and J. Dambre, Improving time series recognition and prediction with networks and ensembles of passive photonic reservoirs, *IEEE J. Sel. Top. Quantum Electron.* **26**, 1 (2020).
- [38] J. Pauwels, G. Van der Sande, G. Verschaffelt, and S. Massar, Photonic reservoir computer with output expansion for unsupervised parameter drift compensation, *Entropy* **23**, 955 (2021).
- [39] B. T. Taddese, T. M. Antonsen, E. Ott, and S. M. Anlage, Sensing small changes in a wave chaotic scattering system, *J. Appl. Phys.* **108**, 114911 (2010).
- [40] B. T. Taddese, G. Gradoni, F. Moglie, T. M. Antonsen, E. Ott, and S. M. Anlage, Quantifying volume changing perturbations in a wave chaotic system, *New J. Phys.* **15**, 023025 (2013).